Article

Understanding the Efficiency of Mn^{4+} Phosphors: Study of the Spinel Mg$_2$Ti$_{1-x}$Mn$_x$O$_4$

Enrique Jara,* Rafael Valiente, Marco Bettinelli, and Fernando Rodríguez*

Read Online

ACCESS | Metrics & More | Article Recommendations

ABSTRACT: We present a spectroscopic study of Mn-doped Mg$_2$TiO$_4$ as a function of pressure and temperature to check its viability as a red-emitting phosphor. The synthesis following a solid-state reaction route yields not only the formation of Mn^{4+} but also small traces of Mn^{3+}. Although we show that Mn^{4+} photoluminescence is not appreciably affected by the presence of Mn^{3+}, its local structure at the substituted Ti^{4+} host site causes a reduction of the Mn^{4+} pumping efficiency yielding a drastic quantum-yield reduction at room temperature. By combining Raman and time-resolved emission and excitation spectroscopies, we propose a model for explaining the puzzling nonradiative and inefficient pumping processes attained in this material. In addition, we unveil a structural phase transition above 14 GPa that worsens their photoluminescence capabilities. The decrease of emission intensity and lifetime with increasing temperature following different thermally activated de-excitation pathways is mostly related to relatively small activation energies and the electric−dipole transition mechanism associated with coupling to odd-parity vibrational modes. A thorough model based on the configurational energy level diagram to the A$_{1g}$ normal mode fairly accounts for the observed excitation and emission—the quantum yield—of this material.

INTRODUCTION

Over the last decade, the search for efficient phosphor-converted white-light-emitting diodes (WLEDs) has become an important issue for scientists and engineers working on materials. In particular, the search for materials with high luminous efficacy and brightness, low power consumption, reliability, long operation lifetime, and environmentally friendly characteristics has been one of the prioritized items in energy-safe devices.[1−6] Traditionally, commercial WLEDs are made by combining green-yellow emitting phosphors (Y$_3$Al$_5$O$_{12}$:Ce^{3+}, YAG:Ce) and a blue (In, Ga)N LED chip (450−480 nm).[7−9] The LED emits blue radiation that is able to excite the green-yellow phosphor yielding an overall white emission. Despite its high efficiency, such phosphors lack an intense red emission (above 600 nm), so the color rendering index is not high enough (CRI < 80) for indoor lighting and the correlated color temperature too high (CCT > 6000 K).[10−14] Therefore, search for efficient red-emitting phosphors that can be excited by blue light is of utmost importance.

The most used elements in the fabrication of red-emitting phosphors are rare-earth (RE) elements, particularly, europium.[15−17] RE elements are scarce and expensive, so their availability to produce inexpensive devices will probably be very limited in the near future. It is then compelling to find suitable RE-free phosphor for WLED technology. Narrow red emission of Mn^{4+} is a promising alternative for RE.[18−20]

It is well known that Mn^{4+} (3d^3) in an octahedral oxygen coordination has three spin-allowed absorption transitions electronic to excited states (the lowest lying ^{4}T$_{2g}$ and two ^{4}T$_{1g}$ at higher energy) that can be efficiently pumped by visible and UV light yielding narrow red emission (strong crystal-field emission: ^{2}E$_g$ → ^{4}A$_{2g}$). Therefore, Mn^{4+}-doped oxide phosphors provide red emission to enhance luminosity in WLEDs.[19,20]

The great chemical and thermal stability of titanate compounds makes them attractive for using as Mn^{4+} host materials in phosphors without charge compensation.[21−23] In particular, Mg$_2$TiO$_4$ has an inverse spinel structure at ambient pressure where Mg^{2+} cations occupy both tetrahedral and octahedral sites, while Ti^{4+} ions sit only at octahedral sites. Thus, it is an ideal matrix to accommodate Mn^{4+} at the strong crystal-field site of Ti^{4+}. Furthermore, the ionic radius of Mn^{4+} (0.53 Å) is similar but shorter than for Ti^{4+} (0.605 Å),[24] providing structural constraints that favor shorter Mn−O bond distances and consequently higher crystal-field strengths at

Figure 1. (a) Room-temperature reflectance spectrum of Mg_2TiO_4:Mn^{4+} (blue line). For comparison, we include the reflectance spectra of a nominally pure Mg_2TiO_4 (gray dashed), Mg_2TiO_4:Mn^{4+} (0.1%) (green dashed line), and Mg_2TiO_4:0.1% Mn^{4+}, 0.5% Bi^{3+}, 0.5% Li^+ (red dashed line) reported elsewhere[28] with permission from Elsevier. (b) Reflectance spectra of the synthesized Mg_2TiO_4:Mn^{4+} for Mn concentrations of 0.1, 0.5, 1.0, and 5.0 mol %. The Mg_2TiO_4:0.1% Mn^{4+}, 0.5% Bi^{3+}, 0.5% Li^+ spectrum (red dashed line)[28] has been included for comparison.

Mn^{4+}. In addition, the replacement of Ti^{4+} by Mn^{4+} avoids charge compensation effects often leading to aggregation or precipitation of dopant ions. These characteristics make Mg_2TiO_4:Mn^{4+} a promising candidate for applications in WLEDs as well as optical thermometry, hydrogen storage, or as a cathode material in lithium-ion batteries.[25]

This work aims at synthesizing the red phosphor Mg_2TiO_4:Mn^{4+} using similar approaches to those followed previously[26–29] and perform a detailed characterization of different manganese valence states and their local structures. It is well known that depending on the synthetic method, manganese can be incorporated mostly as Mn^{4+}, but other oxidation states as Mn^{3+} or Mn^{2+} are also likely. This work also encompasses investigations on the effects of pressure on the structure and photoluminescence properties of Mg_2TiO_4:Mn^{4+} to probe its structural stability and to unveil whether the photoluminescence efficiency is enhanced or deteriorates under high-pressure conditions. We focus on the pressure dependence of electronic and vibrational structures and luminescence lifetime, trying to correlate such variations with interatomic distances, i.e., the actual Mn^{4+}–O^{2-} distance in the substituted TiO_6 octahedron host, Mn^{3+}–Mn^{3+} and Mn^{3+}–Mn^{4+} average distances, etc., to establish structural requirements to be followed for the synthesis of more efficient Mn^{4+} photoluminescence materials.

■ EXPERIMENTAL SECTION

Mg_2TiO_4:Mn^{4+} was synthesized following a solid-state reaction route[26] using TiO_2, $(CH_3COO)_2Mg\cdot4H_2O$ and $(CH_3COO)_3Mn\cdot2H_2O$ as precursors. Stoichiometric amounts of these compounds were weighed for different Mn concentrations (0.1, 0.5, 1.0, and 5.0 mol %) and ground in an agate mortar. After that, they were calcined at 700 °C for 2 h. The resulting product was reground, pressed into a 1 cm diameter pellet (10 tons loading) and reheated up to 1500 °C for 48 h. It was then cooled down to 1000 °C and quenched. This last step was repeated one more time. The cubic spinel phase at ambient conditions was checked by powder X-ray diffraction (XRD) using a Bruker D8 diffractometer and analyzed with the MAUD software.[30] The lattice parameter was $a = 8.441$ Å, similar to the host matrix; thus, Mn doping

below 2 mol % has no measurable effects on the lattice parameter.

A Boehler-Almax diamond anvil cell (DAC) was used for high-pressure studies. 200 μm thick Inconel 625 gaskets were preindented to reduce thickness down to 50 μm. Then, suitable 200 μm diameter holes were perforated with a BETSA motorized electrical discharge machine. The ruby luminescence was used as pressure gauge.[31] Methanol−ethanol (4:1) mixture was used as pressure transmitting media. It must be noted, however, that according to the ruby line broadening, nonhydrostatic effects were insignificant in the explored range, as previously reported.[32]

Reflectance spectra at ambient conditions were obtained with a Cary 6000i UV−vis−NIR spectrophotometer equipped with an integrating sphere over the 200−1700 nm range. Raman spectra were obtained with a BWTEK Raman instrument, consisting of a BRM-OEM-785 diode laser (785 nm), a Prime T BTC661E-785CUST spectrometer with a Hamamatsu CCD (S10141-1107S, 2048 pixels) detector, and a BAC100-785E Raman head equipped with a CCD camera. The selected wavelength prevents unwanted emission from the sample that could hide Raman peaks. The spectrometer was attached through an optical fiber to a confocal microscope equipped with a 20✕ objective. The setup covers the spectral range 80−3600 cm^{-1}, with a spectral resolution of 4 cm^{-1}. The laser power on the sample was kept below 5 mW to avoid heating effects. The luminescence, excitation, and lifetime measurements at ambient conditions were taken with a fluorometer (FLSP920 from Edinburgh Instruments) equipped with a continuous 450 W and a 4 W supercontinuum from Fianium as excitation source, double monochromators, and a Hamamatsu R928P photomultiplier tube (PMT) as a detection system in the visible spectral region. A closed-cycle He cryostat was used for spectroscopic measurements as a function of temperature in the 20−300 K range. For high-temperature measurements (up to 500 K), the sample was placed on a thermally calibrated ceramic resistor. The high-pressure luminescence spectra were obtained by means of an optical-fiber bundle collecting the luminescence of the sample inside the DAC. Emission measurements at high pressure were also carried out by exciting with an optical parametric oscillator (OPO) system (Vibrant II, Opotek) and the luminescence
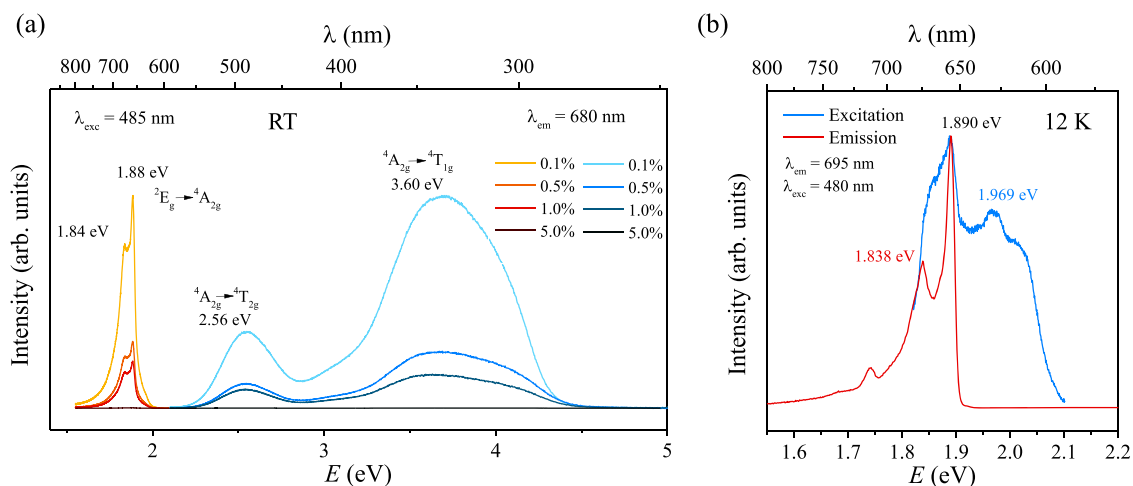
Figure 2. (a) Excitation and emission spectra of $Mg_2TiO_4:Mn^{4+}$ for the different concentrations of Mn (0.1, 0.5, 1.0, and 5.0 mol %) at ambient conditions. (b) 12 K high-resolution emission and excitation spectra around the $^2E_g \leftrightarrow {}^4A_{2g}$ transition.

from the DAC was focused on an optical-fiber bundle attached to a 0.32 m focal monochromator (Horiba-Jobin-Yvon Triax HR 320) equipped with an intensified charge-coupled device (CCD) (iCCD S20 GenII) for detection. Analysis of spectra was performed using Origin and Grams software.

RESULTS AND DISCUSSION

Impurity Characterization. The synthesis of $Mg_2TiO_4:Mn^{4+}$ can stabilize distinct manganese valence states other than Mn^{4+}. Therefore, a thorough characterization of manganese ions formed in Mg_2TiO_4 results crucial given that Mn^{2+}, Mn^{3+}, or Mn^{5+} are all optically active ions, and their presence can significantly affect the photoluminescence (PL) properties of Mn^{4+} and thus the phosphor itself. One advantageous characteristic of manganese ions is the rich peak structure shown by the corresponding excitation/absorption spectra associated with the manifold states arising from the d^n ($n = 2-6$)[33,34] configurations in their different valence states, making it important to identify them by optical spectroscopy.[28,35-37] Figure 1 shows the reflectance spectra of Mg_2TiO_4 singly doped with Mn and triply doped with Mn, Bi, and Li. Interestingly, there is a rich band structure below the host-material band gap (4 eV), being characteristic of the manganese valence state. Thus, the two bands at 2.48 eV (500 nm) and 3.26 eV (380 nm) in $Mg_2TiO_4:0.1\%$ Mn^{4+}, 0.5% Bi^{3+}, and 0.5% Li^+ are related to the $^4A_{2g} \rightarrow {}^4T_{2g}$ and $^4T_{1g}$ crystal-field intraconfigurational transitions of Mn^{4+} ($3d^3$) in octahedral coordination. On the other hand, the singly doped $Mg_2TiO_4:Mn^{4+}$ shows a broad band centered at 1.23 eV (1010 nm) and two Mn^{4+}-related weak absorption bands (not visible in Figure 1) at 2.48 eV (500 nm) and 3.26 eV (380 nm); the intensities of the latter ones being 7 times smaller than those observed in the sample doped with Li^+ and Bi^{3+} and the same Mn concentration $x = 0.001$ (0.1 mol %). We associate the broad band at 1.23 eV—the major feature of the reflectance spectra—to Mn^{3+}. In particular, this band is assigned to the $^5B_{1g} \rightarrow {}^5A_{1g}$ transition, corresponding to the parent octahedral ^5E_g state split by the low-symmetry crystal-field distortion due to the Jahn–Teller effect into $^5B_{1g}$ and $^5A_{1g}$ states.[36,38,39]

Although two absorption bands at 2.48 and 3.26 eV were clearly observed by Qiu et al.[28] in $Mg_2TiO_4:0.1\%$ Mn^{4+}, 0.5% Bi^{3+}, 0.5% Li^+, we barely observe these bands in our singly

doped $Mg_2TiO_4:Mn^{4+}$; the reflectance spectrum of which is dominated by the broad band at 1.23 eV. Despite the severe intensity reduction of Mn^{4+} absorption bands in the singly doped $Mg_2TiO_4:Mn^{4+}$ compared to the triply doped with Mn, Li, and Bi samples, the former shows an intense Mn^{4+}-related PL emission under excitation at 3.70 or 2.56 eV (335 or 485 nm). In fact, its characteristic narrow-band red PL is due to octahedral Mn^{4+}, as it is confirmed through the corresponding excitation spectrum showing the two bands at 2.56 eV (485 nm) and 3.60 eV (344 nm) at room temperature (Figure 2a).

These excitation and emission spectra are typical of Mn^{4+} in oxides.[40] Excitation into any of these bands induces narrow-band PL associated with the $^2E_g \rightarrow {}^4A_{2g}$ emission, consisting of two main overlapping peaks at 1.84 and 1.88 eV—674 and 659 nm, respectively—at room temperature. Their intensity decreases with increasing the manganese concentration from 0.1 to 5 mol % (Figure 2a). The emission and the corresponding mirrorlike excitation spectra are better resolved at low temperatures (Figure 2b). The two emission components slightly shift to higher (shorter) energies (wavelengths) at 1.838 and 1.890 eV (674.5 and 656.0 nm) at 12 K, whereas they appear at 1.890 and 1.969 eV (674.5 and 629.7 nm) in excitation. It turns out that the 1.890 eV peak corresponds to the zero-phonon line, from which two odd-parity vibronic components are observed at 1.838 eV in emission and 1.969 eV in excitation, with associated coupled phonons of 52 meV (ground state) and 80 meV (excited state), respectively. Similar vibronic components in excitation/emission associated with the ^2E_g state have been experimentally observed in other Mn^{4+} systems.[40] We associate 52 meV (419 cm^{-1}) and 80 meV (645 cm^{-1}) phonons with the $\nu_4(t_{1u})$ and $\nu_3(t_{1u})$ modes, which were observed at 44 meV (355 cm^{-1}) and 81 meV (655 cm^{-1}) in fluorides, respectively.[40] Nevertheless, the broad shoulder around 2.0 eV observed in excitation can be due to transitions to the nearby $^2T_{1g}$ excited state. The energy difference between the zero-phonon line and the shoulder centroid (110 meV) is consistent with the estimated energy difference as a function of Racah parameters B and C, and the crystal-field splitting Δ, as $E(^2T_{1g}-{}^2E_g) = 1.0B = 100$ meV for $B = 100$ meV (807 cm^{-1}) and $C/B = 4.1$, as derived from excitation and emission peak energies.[19,41,42] These values were obtained by eqs 1, 2, and 3[41]

$$B = \frac{\Delta(\beta^2 - 10\beta)}{150(\beta - 8)} \tag{1}$$

with

$$\beta = 10\left[\frac{E(^4T_{1g})}{\Delta} - 1\right] \tag{2}$$

$$3.05\frac{C}{B} = 18\frac{B}{\Delta} - 7.09 + \frac{E(^2E_g)}{B} \tag{3}$$

using the experimental data $\Delta = E(^4T_{2g}) = 2.56$ eV, $E(^4T_{1g}) = 3.60$ eV, and $E(^2E_g) = 1.890$ eV. It is worth mentioning that the factor 7.09 in eq 3 is often wrongly written as 7.90 in the literature,[27,41,43-47] probably due to a typographical error in the widely cited equation from the textbook by Henderson and Imbusch, who reported a value of 7.90 instead of 7.09 in eq 9.2 elsewhere.[43] The diagonalization of the ^2E manifold state matrix within the d^3 electronic configuration yields the correct factor 7.09[48] in eq 3, so that providing an approximate energy (within less than 1%) of the lowest energy $E(^2E_g)$ state in the range $15 < \Delta/B < 35$ and $3 < C/B < 5$.[43]

The time-dependence emission intensity, $I(t)$, varies with the manganese concentration, its lifetime decreasing with increasing the concentration (Figure 3). Although it is a
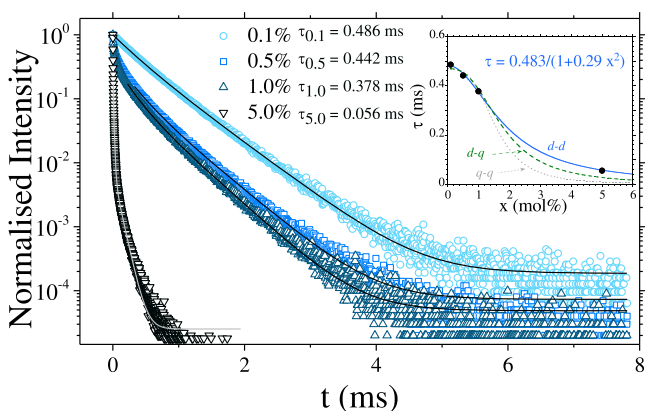
Figure 3. Decay times of Mg_2TiO_4:Mn^{4+} for the different concentrations of Mn (0.1, 0.5, 1.0, and 5.0 mol %). The inset shows the lifetime vs concentration data and corresponding fits to transfer mechanisms via dipole−dipole (d−d), dipole−quadrupole (d−q), and quadrupole−quadrupole (q−q).

general well-known behavior that the PL lifetime of transition-metal ions decreases with increasing the activator concentration due to energy transfer and excitation capture by nonradiative impurities,[19,29,43,49] the decrease of PL intensity observed here does not match the corresponding lifetime decrease (Figures 2 and 3). In fact, the lifetime decrease can be described in terms of a de-excitation probability proportional to the square of the Mn^{4+} concentration. This behavior is characteristic of concentration-dependent nonradiative processes involving a critical distance for transfer and subsequent trapping to non-PL impurities through a dipole−dipole mechanism.[50] The reduction of PL intensity with the manganese concentration is actually more pronounced than the one expected on the basis of the lifetime decrease due to nonradiative processes (Figure 4b). According to the PL quantum yield derived from the PL lifetime (eq 4), the maximum PL intensity would be expected for a manganese

concentration $x = 1$ mol % that is an order of magnitude higher than the concentration providing the maximum PL ($x = 0.1$ mol%). This simple result unravels that additional nonradiative channels other than ^2E_g must be involved in the excitation dynamics of Mn^{4+}. As it is shown below, we associate this unexpected behavior to nonradiative multiphonon de-excitation from the pumping $^4T_{2g}$ state to the $^4A_{2g}$ ground state in competition with the multiphonon relaxation to the ^2E_g emitting state.

First, we consider the possible effect of Mn^{3+} in the Mn^{4+} PL efficiency in a sample containing both Mn^{4+} and Mn^{3+} ions, as a possible nonradiative channel via direct energy transfer from Mn^{4+} to the luminescence quencher Mn^{3+}. Although Mn^{3+} is known to act as a PL killer in Mn^{2+} compounds,[49] this mechanism is ruled out for Mn^{4+} since the ^2E_g emitting excited state does not match with the Mn^{3+} absorption, and its lifetime is not significantly affected by the Mn^{3+} between $x = 0.1-1$ mol %, although Mn^{3+} concentration increases by a factor 3 (Figure 4a). The PL intensity can thus be modeled through the following eqs 4, 5, and 6

$$\eta_{PL_{2E}} = \tau_r^{-1}/(\tau_r^{-1} + \tau_{nr}^{-1}) \tag{4}$$

$$\eta_{pumping} = I_0 \cdot \sigma_{abs} \cdot \phi_{pumping} \tag{5}$$

$$I^{Mn^{4+}} = [Mn^{4+}] \cdot \eta_{pumping} \cdot \eta_{PL_{2E}} \tag{6}$$

The first two equations represent the PL quantum yield of the ^2E_g emitting state of Mn^{4+} and the pumping efficiency, i.e., transfer efficiency from the pumped $^4T_{2g}$ excited state to the ^2E_g emitting state, respectively. In the second equation, I_0 and σ_{abs} are the pumping intensity and the absorption cross section, respectively, while $\phi_{pumping}$ is the fraction of multiphonon relaxation from the pumped $^4T_{2g}$ to the ^2E_g emitting state. This fraction is 1 if all $^4T_{2g}$ excited states relax into the ^2E_g state. The transition probability—the reciprocal lifetime—is given by $\tau^{-1} = \tau_r^{-1} + \tau_{nr}^{-1}$, where τ is the PL decay lifetime at a given pressure and temperature and τ_r^{-1} and τ_{nr}^{-1} are the radiative and nonradiative probabilities, respectively. The third equation is the PL intensity of Mn^{4+}, which is proportional to $[Mn^{4+}]$ concentration.

It is important to remark that an adequate model to account for excitation and PL intensities requires knowing the total concentration of Mn^{4+} or the fraction of manganese concentration entering as Mn^{4+}. To do so, we have estimated the Mn^{3+} concentration as a function of the nominal concentration of manganese x, on the assumption that the extinction coefficient at the maximum of the 1010 nm band is $\epsilon = 100$ M^{-1} L cm^{-1}, as it was measured for 6-fold coordinated $Mn^{3+}O_6$ in epidote.[36] The so-obtained $[Mn^{3+}]$ from the spectra of Figure 1 is shown in Figure 4a. Although $[Mn^{3+}]$ increases with x, it is an order of magnitude smaller than x, thus indicating that $[Mn^{4+}]$ is about 90% of the nominal manganese concentration under the synthetic conditions used in this work.

These data are worth unraveling the different absorption cross section (transition oscillator strength) associated with the crystal-field transitions of Mn^{4+} in Mg_2TiO_4:0.1% Mn^{4+}, 0.5% Bi^{3+}, 0.5% Li^+,[28] and Mg_2TiO_4:0.1% Mn^{4+} reported in this work. While in the former, Mn^{4+} absorption bands are clearly visible, they are barely observed in the latter, the absorption coefficients of which are 7 times smaller, in spite of the fact that $[Mn^{4+}]$ is similar in both systems. In line to explanations
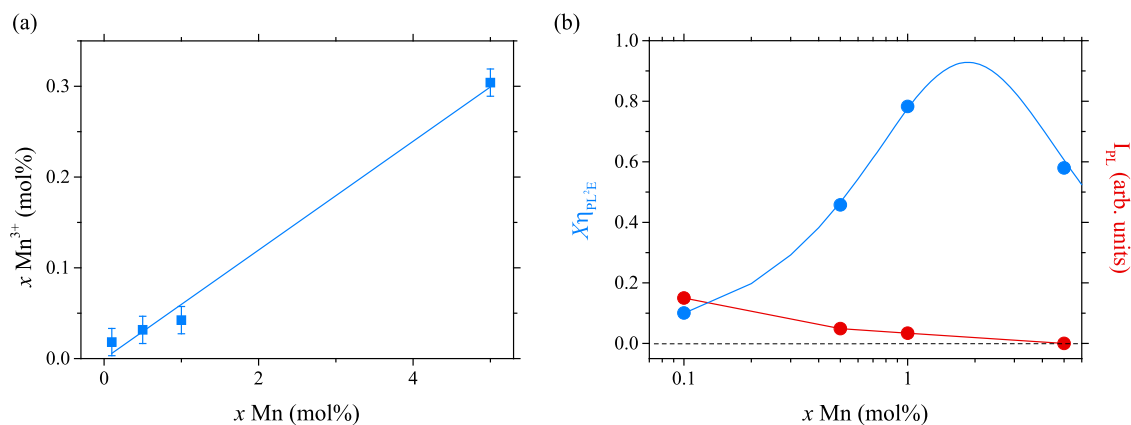
Figure 4. (a) Mn^{3+} concentration in $Mg_2Ti_{1-x}Mn_xO_4$ as a function of the nominal manganese concentration, x, derived from the absorption coefficient of the 1.23 eV (1010 nm) absorption band. (b) Comparison between the x-dependence of the Mn^{4+} PL intensity measured upon excitation at 485 nm (red dots) and the calculated one (blue dots) through the PL quantum yield using the measured PL lifetime (eqs 4−6).
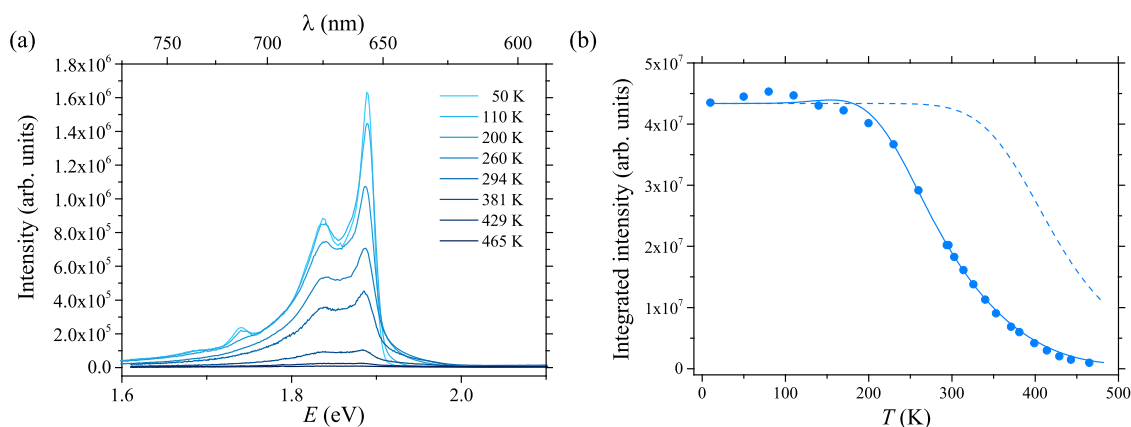

Figure 5. (a) Temperature dependence of the PL emission spectrum (λ_{exc} = 480 nm). (b) Variation of the integrated emission intensity with temperature. The dotted line corresponds to the expected temperature-dependence intensity based on the measured lifetimes of ^2E_g and eqs 4−6. The continuous line includes an additional nonradiative multiphonon from the pumped $^4T_{2g}$ state (see text in the last section for explanation).

given elsewhere,[28] here we conclude that the pumping enhancement attained in the triply doped system with respect to the simply doped one is due to the increase in the Mn^{4+} absorption cross section caused by the loss of center of inversion in $Mn^{4+}O_6$ by the nearby presence of Bi^{3+} and Li^+. Rather than vibronic-induced enhancement,[28] we interpret the increase of oscillator strength, hence the pumping capability, in Mg_2TiO_4:0.1% Mn^{4+}, 0.5% Bi^{3+}, and 0.5% Li^+ by the noncentrosymmetric crystal-field static perturbation in Mn^{4+} produced by such nearby ions. These results are supported by a recent study in Mg_2TiO_4:Mn^{4+} using Ca^{2+}, Sr^{2+}, Ba^{2+}, Li^+, Na^+, or Al^{3+} as codopant ions.[51] These effects are important to understand why the Mn-concentration dependence of the PL intensity does not scale with the corresponding lifetime measurements following eq 4 and is 7 times weaker than the PL intensity attained in the triply doped crystal for the same Mn^{4+} concentration of 0.1 mol %. Besides, the expected concentration dependence of the emission intensity does not match the observed intensity. It implies the presence of other nonradiative de-excitation mechanisms, which are not reflected in the x-dependence of the PL lifetime. Figure 4b compares the x-dependence of the measured and calculated PL intensity under excitation at 485 nm according to the variation of the PL lifetime with concentration considering both radiative and nonradiative probabilities (eq 4). Whereas the presence of

Mn^{3+} does not appreciably affect the PL lifetime, the loss of PL efficiency with x is beyond the nonradiative mechanism involved in the de-excitation dynamics of the ^2E_g state. These additional x-dependent nonradiative channels seem to be responsible for the best PL efficiency attained in the Mn(0.1 mol %)-doped phosphor. In the sections below, we will show that such nonradiative channels involve the $^4T_{2g}$ rather than the ^2E_g excited state.

Figure 5 shows the temperature dependence of the characteristic $^2E_g \rightarrow {}^4A_{2g}$ emission spectra in Mg_2TiO_4:0.1% Mn^{4+} upon excitation into the $^4T_{2g}$ level at 480 nm in the 10−500 K range. Its integrated band intensity, $I_{PL}(T)$, exhibits a strong dependence on temperature. It slightly increases with temperature from low temperature, reaching a maximum at 80 K, above which the intensity decreases smoothly up to about ~250 K, and abruptly above this temperature, following an Arrhenius-type behavior, characteristic of a thermally activated process. It must be noted that the two vibronic replicas forming the luminescence spectra become unresolved above 400 K due to thermal peak broadening. Thus, this behavior suggests that $^2E_g \rightarrow {}^4A_{2g}$ de-excitation involves both radiative and nonradiative processes, the latter increasing with temperature with an associated quenching temperature (the temperature at which $I_{PL}(T_Q) = I_{PL}(0)/2$)[52] of T_Q = 300 K. It is worthwhile noting that $I_{PL}(T)$ does not scale with the

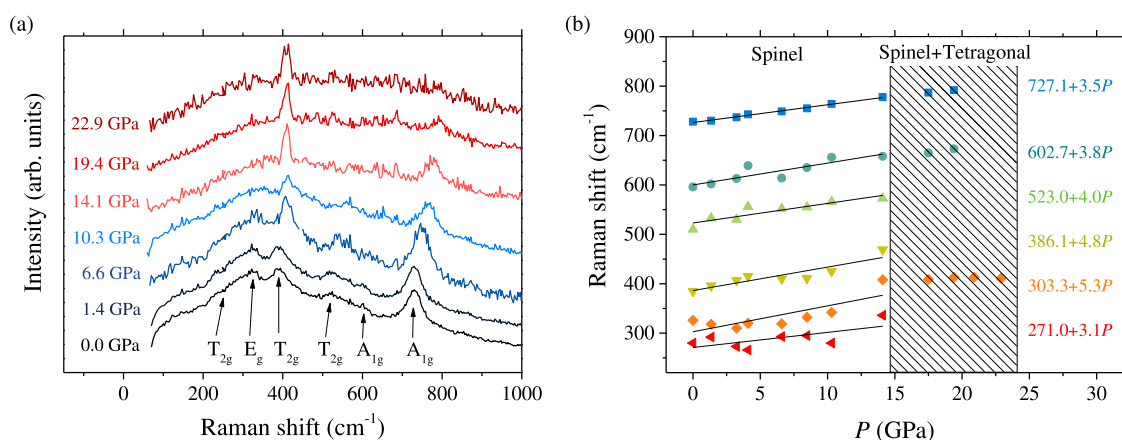**Figure 6.** (a) Pressure dependence of the Raman spectrum in Mg_2TiO_4:0.1% Mn^{4+}. The spectra show the six peaks associated with the corresponding Raman active modes of the inverse spinel structure. Mode labels are indicated by arrows following assignments given elsewhere.[54] (b) Variation of the vibrational frequencies with a pressure of the six Raman modes. The least-square linear fit equations $\nu(P) = \nu_0 + (d\nu/dP)P$ in the spinel phase are included on the right side. The frequency uncertainty is within the symbol size.

luminescence quantum efficiency as deduced from the temperature dependence of the lifetime $\tau(T)$ following eq 1. The dashed curve of Figure 5b corresponds to the expected $I_{PL}(T)$ as $I_{PL}(0) \times \eta PL_{2E}(T)$ using the measured lifetime data $\tau(T)$ and eq 4. The comparison of the expected and measured $I_{PL}(T)$ clearly indicates that the intensity drop above 300 K is not conveyed in the lifetime data, and thus some other nonradiative de-excitation processes must be involved. The uncorrelated temperature behavior of $\tau(T)$ and $I_{PL}(T)$ is not new as it has been observed in several Mn^{4+} systems; however, its cause has not been properly addressed so far. Interestingly, here we interpret this phenomenon in terms of a loss of pumping efficiency of the ^2E_g emitting state (eq 5) due to competing relaxation mechanisms from $^4T_{2g}$ to ^2E_g and directly to the $^4A_{2g}$ ground state. As it is explained in the following sections, the singular electronic structure of Mn^{4+} in oxides and fluorides[19,20,42] favors this direct relaxation mechanism. The experimental $I_{PL}(T)$ data have been accounted for by including such an additional nonradiative mechanism as showed by the continuous curve of Figure 5b. The enhancement of such direct nonradiative de-excitation channel, which has been also observed in other works,[52,53] limits the potential of these materials for applications as phosphors.

Crystal Structure and Luminescence under High-Pressure Conditions. *Raman Spectroscopy.* The structural stability of Mg_2TiO_4:0.1% Mn^{4+} has been explored as a function of pressure up to 23 GPa by Raman spectroscopy. The spectrum at ambient conditions shows six Raman active modes ($3T_{2g} + 1E_g + 2A_{1g}$) according to the $Fd3m$ space group of the spinel structure (Figure 6).[54]

The higher-frequency A_{1g} peaks at 727 and 603 cm^{-1} correspond to stretching modes of the MgO_4 tetrahedra. The E_g mode at 303 cm^{-1} is related to symmetric bending vibrations of oxygens, whereas the T_{2g} mode near 523 cm^{-1} to an asymmetric bending of O–Mg–O bonds. The second T_{2g} mode with a frequency of 271 cm^{-1} is related to translations of the TiO_6 octahedra with respect to Mg^{2+} cations. The third T_{2g} mode at 386 cm^{-1} involves opposing translations of the cations and oxygens along one lattice direction. The variation of the Raman spectrum with pressure is shown in Figure 6. Within the experimental uncertainty, we observe that all Raman frequencies increase linearly with pressure up to 14.1 GPa with pressure coefficients ranging from 3.1 to 5.3 cm^{-1} GPa^{-1}, i.e.,

Grüneisen parameters from 0.81 to 2.95. Table 1 summarizes the frequencies and mode assignment of the observed Raman

Table 1. Experimental Raman Mode Frequency, ν_0, and Pressure Coefficient ($d\nu/dP$), Derived by Fitting the Experimental Data $\nu(P)$ to the Equation $\nu(P) = \nu_0 + (d\nu/dP)P$, Together with the Grüneisen Parameter (γ) of Mg_2TiO_4:0.1% Mn^{4+} [a]

mode	ν_{Wang}[54] (cm^{-1})	ν_0 (cm^{-1})	$d\nu/dP$ (cm^{-1}/GPa^{-1})	$\gamma = (K_0/\nu)$ $d\nu/dP$
T_{2g}	281	271	3.1	1.90
E_g	326	303	5.3	2.90
T_{2g}	385	386	4.8	2.06
T_{2g}	506	523	4.0	1.27
A_{1g}	596	603	3.8	1.05
A_{1g}	728	727	3.5	0.81

[a]The Grüneisen parameters have been derived from the corresponding bulk modulus (K_0) of the inverse spinel structure $K_0 = 169$ GPa.[55]

peaks following previous studies on Mg_2TiO_4,[54] as well as their pressure coefficients and Grüneisen parameters. Above 14 GPa, the crystal undergoes a structural phase transition yielding the coexistence of spinel and tetragonal phases in a wide pressure range up to 24.3 GPa.[54] The Raman spectrum in the phase coexistence region becomes unresolved due to peak overlap and only E_g and $2A_{1g}$ modes could be spectroscopically resolved. It must be noted that the measured frequencies are slightly shifted toward higher energies with respect to those previously reported for nominally pure Mg_2TiO_4.[54] In particular, these differences are larger for low-frequency modes, where their Grüneisen parameters show significant discrepancies. Such frequency deviations can be related to lattice distortions induced by doping with manganese due to the smaller size of Mn^{4+}.

Luminescence Properties. The variation of the PL emission and corresponding excitation spectra with pressure is shown in Figure 7. They allow us to follow the evolution of the three peaks involved in the $^2E_g \rightarrow {}^4A_{2g}$ emission transition as well as the crystal-field splitting, $\Delta (=10Dq)$, through the excitation transition of Mn^{4+} in Mg_2TiO_4:0.1% Mn^{4+} up to 14 GPa in the spinel phase.
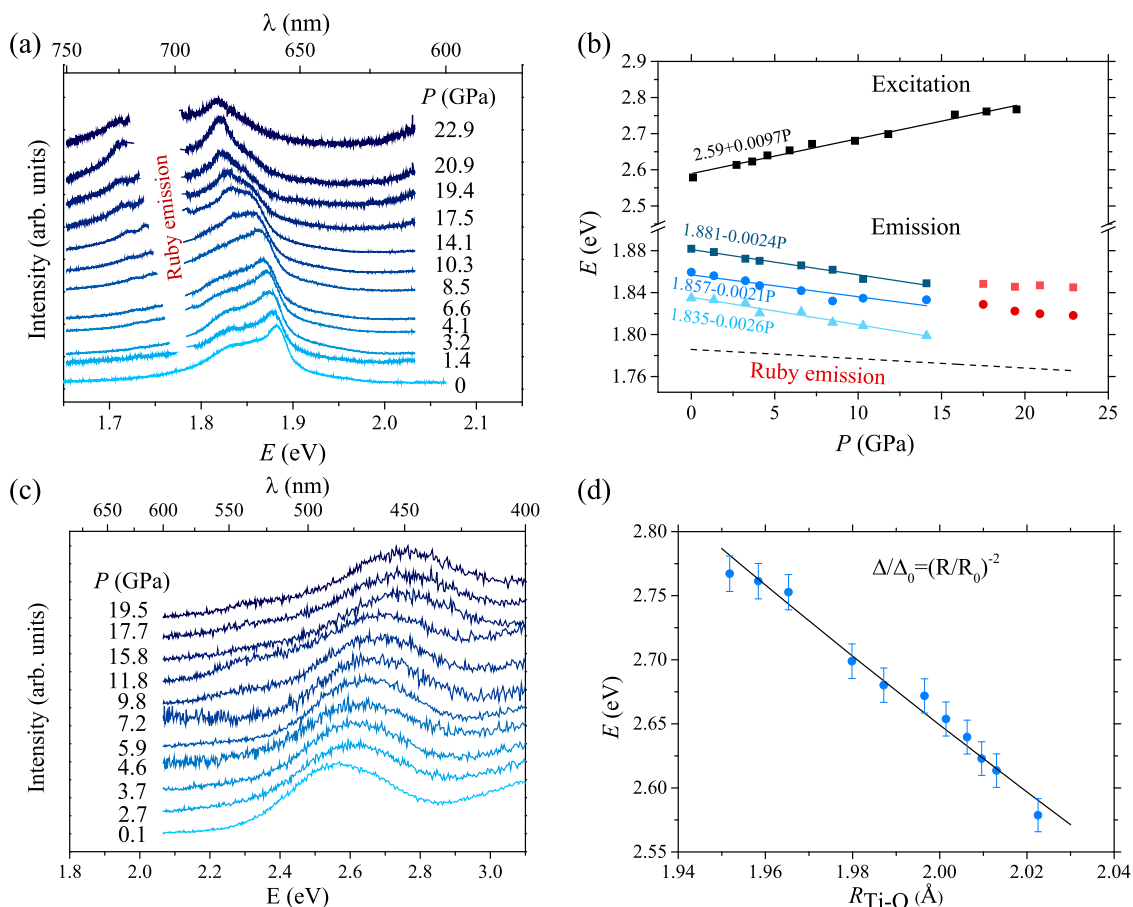
Figure 7. (a) Pressure dependence of the emission spectrum of Mg_2TiO_4:0.1% Mn^{4+} (λ_{exc} = 480 nm). (b) Energy variation of three components of the ^2E_g emission and the corresponding $^4T_{2g}$ excitation of Mn^{4+} with pressure. Note that the energy scale for emission is 4 times the excitation energy scale. Straight lines correspond to the least-square linear fits to $E(P)$. (c) Pressure dependence of the excitation spectrum of Mg_2TiO_4:0.1% Mn^{4+} (λ_{em} = 660 nm). (d) Variation of the $^4T_{2g}$ excitation band energy as a function of the Ti–O distance, $R_{Ti–O}$, derived from the equation of state of Mg_2TiO_4.[54] The line corresponds the fit of experimental data to a potential law (see text). In terms of pressure: $E(P)$ = 2.59 + 0.0097P (in eV and GPa units).

The emission spectrum at 50 K consists of a zero-phonon line at 656 nm (1.890 eV)—being the most intense component—followed by two replicas at 668 nm (1.856 eV) and 674.5 nm (1.838 eV) arising from electron−phonon coupling of the zero-phonon line to odd-parity vibrations with frequencies of 194 cm^{-1} (24 meV) and 371 cm^{-1} (46 meV), respectively. This assignment is based on the fact that such three components decay following the same time dependence and thus arising from the same Mn^{4+} center and are also observed as anti-Stokes components of the zero-phonon line in the excitation spectrum at 50 K; the displacements of which are 103 cm^{-1} (12.8 meV) and 419 cm^{-1} (52 meV), respectively. A similar vibronic structure around the zero-phonon line has also been observed in Mn^{4+}-doped fluorides.[19] In fact, the odd vibration frequencies derived from the ambient pressure emission spectrum of Mg_2TiO_4:0.1% Mn^{4+} are close to the $\nu_6(t_{2u})$ and $\nu_4(t_{1u})$ mode frequencies of 240 cm^{-1} (29.7 meV) and 355 cm^{-1} (44.0 meV), respectively, measured by infrared spectroscopy.[19] Similarly to Cr^{3+} ($3d^3$) in ruby, emission peaks in Mg_2TiO_4:0.1% Mn^{4+} red-shift with pressure (toward lower energies) with pressure coefficients of 2.6, 2.1, and 2.4 meV GPa^{-1}, respectively, all being at least twice the rate of the ruby emission shift of 0.97 meV GPa^{-1} (0.364 nm GPa^{-1}).[31] Above 14 GPa, the lowest energy emission component (675.5 nm) is no longer observable, the peak at

668 nm becoming the major feature of the emission spectra, while the zero-phonon line at 659 nm appears as a shoulder of the major component. This change as well as the loss of spectral resolution correlates with the coexistence of the spinel and tetragonal phases in this pressure range as Raman spectroscopy shows.

Figure 7c shows the variation of first Mn^{4+} excitation band $^4A_{2g} \rightarrow {}^4T_{2g}$ in Mg_2TiO_4:0.1% Mn^{4+} with pressure. According to trends of the Tanabe−Sugano diagram for d^3 ions, the energy of this band provides the crystal-field splitting between the 3d orbitals e_g−t_{2g}, Δ. The band blue-shifts with pressure assuming a similar behavior of Ti−O and Mn−O distances, i.e., upon reduction of the Ti−O bond length, $R_{Ti−O}$, following a potential law as $\Delta = \Delta_0(R_{Ti−O}/R_0)^{-n}$,[36,56] with Δ_0 and R_0 being the ambient pressure crystal-field splitting and $R_{Ti−O}$, respectively. The fit of experimental data to this potential law provides values of Δ_0 = 2.59 eV, R_0 = 2.02 Å, and n = 2. According to crystal-field models[56] and experimental results in oxides[44] and fluorides,[57−59] typical values of n are around 5. This large deviation between the expected and measured exponent can be attributed to the different Mn−O distance and bond compressibility with respect to the host Ti−O values. In fact, the Ti−O distance is expected to be about 0.07 Å longer than the Mn−O distance taking into account the ionic radius difference.[24] It means that an inward relaxation of
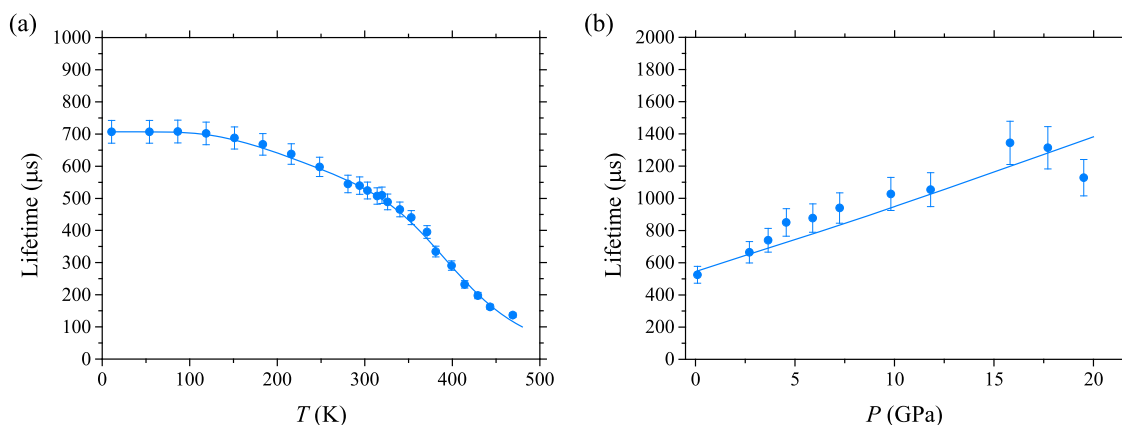
Figure 8. Decay times of Mg_2TiO_4:0.1% Mn^{4+} under excitation λ_{ex} = 480 nm. (a) Ambient pressure, temperature-dependent luminescence decay time. (b) Pressure dependence of the luminescence decay time at room temperature. Solid curves represent the theoretical dependence given by eq 9.

the MnO_6 octahedron toward a more compressed octahedron—shorter Mn−O bond length—yields smaller local compressibility with respect to the host TiO_6 octahedron. Both effects can modify the exponent of the potential law when replacing R_{Ti-O} by the real Mn−O distance, R. Assuming that the lattice relaxation around the Mn^{4+} impurity in Mg_2TiO_4:Mn^{4+} leads to an impurity-oxygen distance R, this should be intermediate between that of the host Ti−O distance in Mg_2TiO_4 (R_{Ti-O} = 2.02 Å) and the Mn−O distance corresponding to the sum of O^{2-} and Mn^{4+} ionic radii (R_{Mn-O} = 1.95 Å). We can define the relaxation parameter (α) as: ($R - R_{Ti-O}$) = $\alpha(R_{Mn-O} - R_{Ti-O})$. Now, if we rescale the real potential law with $n = 5$ by replacing R with R_{Ti-O}, then we get $\Delta = \Delta_0(R_{Ti-O}/R_0)^{-5\alpha}$. A value of $\alpha = 0.4$ would account for the measured exponent. It means that the real Mn−O distance in Mg_2TiO_4:0.1% Mn^{4+} would be R_{Mn-O} = 1.99 Å at ambient conditions; the $Mn^{4+}O_6$ octahedron is stiffer than the host $Ti^{4+}O_6$ one.

De-Excitation Dynamics: Lifetime Measurements. Figure 8a shows the Mn^{4+} PL time dependence in Mg_2TiO_4:0.1% Mn^{4+}—the most efficient doping concentration of the series—as a function of temperature. All decay curves display a similar single exponential behavior with an associated lifetime strongly dependent on the Mn concentration at temperatures above 100 K. Its variation resembles that the PL intensity $I_{PL}(T)$ of Figure 5b, although the decrease of $I_{PL}(T)$ with temperature unveils additional nonradiative mechanisms other than those involved in $\tau(T)$. The continuous curve of Figure 5b simulates the variation of $I_{PL}(T)$ on the basis of the variation of $\tau(T)$ as it is discussed below. The loss of intensity and the concomitant lifetime decrease with temperature are associated with the nonradiative process arising mainly from the pumped $^4T_{2g}$ excited state, having a distinct manifestation in $I_{PL}(T)$ and $\tau(T)$. Here, we show that the variations of $I_{PL}(T)$ and $\tau(T)$ unravel nonradiative mechanisms, which affect both the $^4T_{2g}$ multiphonon process into the ^2E_g emitting state (pumping efficiency) in competition with a direct multiphonon de-excitation into the $^4A_{2g}$ ground state or an energy transfer to other neighboring Mn^{4+}, and the ^2E_g de-excitation dynamics (PL efficiency), all affecting $I_{PL}(T)$, but the latter mechanism affecting only $\tau(T)$. The analysis of these two processes is noteworthy since both influence the PL quantum yield of the phosphor.

First, the relaxation dynamics of the ^2E_g emitting state is well described in terms of two different de-excitation pathways: (1) a radiative probability governing the low-temperature lifetime behavior, τ_{rad}^{-1}, and (2) a nonradiative de-excitation process, including all de-excitation channels such as multiphonon relaxation, energy transfer, excited-state absorption, etc., which are mainly responsible for the lifetime decrease at higher temperatures (above 250 K) and the concomitant loss of PL intensity. In the former case, the radiative probability is simultaneously activated by spin−orbit coupling that relaxes the spin-forbidden nature of the electric−dipole transition (eq 7) and odd-parity vibrations that enable mixing of the ^2E_g and $^4T_{2g}$ excited states with odd-parity charge-transfer states, making the transition parity and spin allowed (eq 8)

$$\tau_0^{-1} = \tau_E^{-1} + \tau_T^{-1}\left(\frac{\Delta E}{\Delta E + \beta P}\right)^2 \tag{7}$$

$$\tau_{rad}^{-1}(T) = \tau_0^{-1} \coth\left(\frac{\hbar\omega_u + \alpha P}{2k_B T}\right) \tag{8}$$

Here, ΔE = 0.706 eV (5695 cm^{-1}) is the energy difference between ^2E_g and $^4T_{2g}$ obtained from the excitation and PL spectra, respectively, τ_E^{-1} and τ_T^{-1} are the radiative probabilities associated with pure ^2E_g and spin−orbit mixed $^4T_{2g}$ coefficients of the emitting ^2E_g wave functions,[60] and $\hbar\omega_u$ = 420 cm^{-1} is the effective fit odd-parity enabling mode frequency, which is no far from the vibrational odd mode frequencies $\nu_3(t_{1u})$ of 655 cm^{-1} (81.2 meV) and $\nu_4(t_{1u})$ of 355 cm^{-1} (44.0 meV) measured in Mg_2TiO_4;[40,54,61,62] β = 0.025 eV GPa^{-1} (200 cm^{-1} GPa^{-1}) is the pressure coefficient of the energy difference $^4T_{2g}$−^2E_g—difference of their respective pressure coefficients (Figure 7b); and α = 0.5 meV GPa^{-1} (4 cm^{-1} GPa^{-1}) is the pressure coefficient obtained from the variation of Raman/IR spectra with pressure (Table 1).[54]

The nonradiative de-excitation mechanism, having a strong influence on the lifetime over 250 K, is described by a thermally activated process depending on the pressure with a probability τ_1^{-1} $e^{-(E_{act}+\gamma P)/k_B T}$, with E_{act} being the activation energy. Within a semiclassical configurational coordinate model, it corresponds to the energy difference between the ^2E_g minimum and the crossing point of the configurational mode parabola of the excited ^2E_g and ground $^4A_{2g}$ states
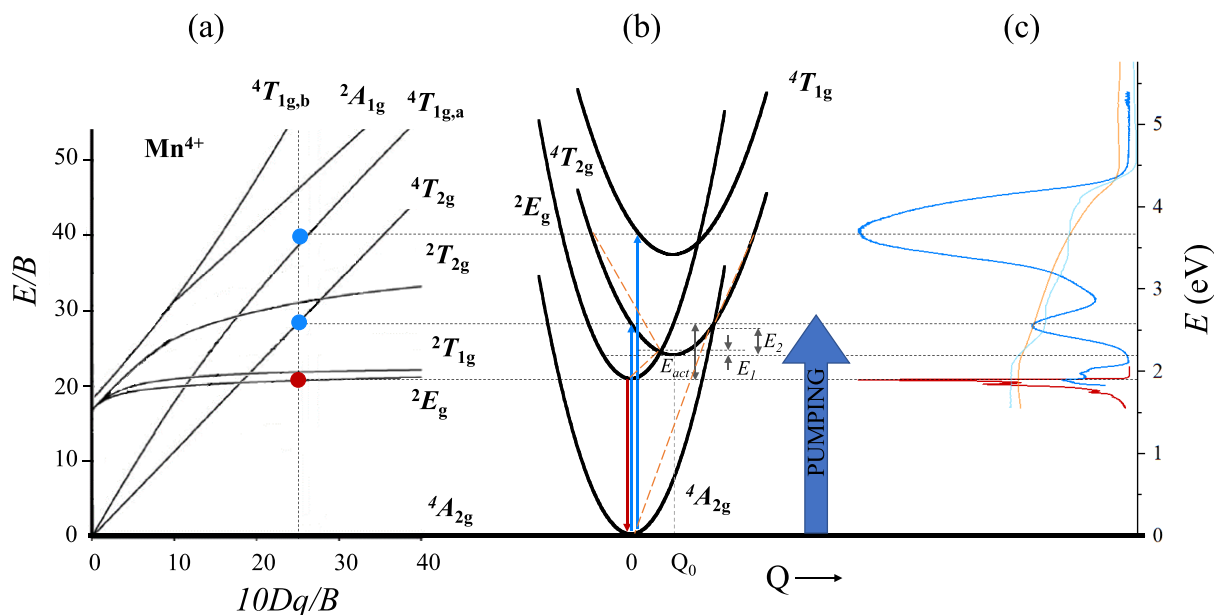
Figure 9. (a) Tanabe−Sugano energy level diagram for a 3d^3 system in octahedral symmetry (Mn^{4+}). (b) Configurational coordinate model representing PL and PLE processes as well as different de-excitation pathways after the pumping. (c) PL (red), PLE (blue), and reflectance (light orange) spectra of Mg$_2$TiO$_4$:0.1% Mn^{4+}, and reflectance spectra of Mg$_2$TiO$_4$:0.1% Mn^{4+}, 0.5% Bi^{3+}, and 0.5% Li$^+$ (light blue).

(Figure 9). Overall, the temperature and pressure dependence of the PL lifetime can be described eq 9

$$\tau^{-1} = \left[\tau_E^{-1} + \tau_T^{-1}\left(\frac{\Delta E}{\Delta E + \beta P}\right)^2\right]\coth\left(\frac{\hbar\omega_u + \alpha P}{2k_B T}\right) + \tau_1^{-1}$$
$$e^{-(E_{act}+\gamma P)/k_B T} \tag{9}$$

In this equation, we have omitted the radiative term associated with $^4T_{2g} \rightarrow {}^4A_{2g}$ emission. Although the thermal population of the $^4T_{2g}$ excited state can be important in Cr^{3+}-doped fluorides like LiCaAlF$_6$ due to the proximity of the energy minima of the corresponding parabola, i.e., the energy difference of the corresponding zero-phonon lines: $\Delta E_{ZPL} = E_{ZPL}(^4T_{2g}) - E_{ZPL}(^2E_g)$,[63] in Mg$_2TiO_4$:0.1% Mn^{4+}, this energy is $E_{ZPL} = 0.36$ eV (2904 cm^{-1}) making the $^4T_{2g}$ population negligible to produce detectable effects on $\tau^{-1}(T)$. The variation of the lifetime with temperature (a) and pressure (b) of Mg$_2$TiO$_4$:0.1% Mn^{4+} shown in Figure 8 has been accounted for by this model. The curves correspond to the fit of eq 9 to the measured $\tau^{-1}(T,P)$ data providing values of $E_{act} = 0.36$ eV, $\tau_T = 708$ μs, $\tau_E = 5$ ms, $\tau_1 = 0.021$ μs, and $\gamma = 36$ meV GPa^{-1} (290 cm^{-1} GPa^{-1}). It must be noted that the obtained E_{act} is in agreement with the activation energy deduced from the configurational energy model of Figure 9 ($E_{act} = 0.31$ eV) that was drawn from spectroscopic data. Interestingly, the obtained E_{act} coincides with the zero-phonon line energy differences, $\Delta E_{ZPL}(^4T_{2g}-^2E_g) = 0.36$ eV. It means that thermal population into $^4T_{2g}$ yielding nonradiative de-excitation directly from $^4T_{2g} \rightarrow {}^4A_{2g}$ is highly probable. The good agreement between spectroscopic and lifetime data together with the adequacy of eq 9 to describe both pressure and temperature dependencies of the lifetime supports the consistency of the model.

The general trend of $\tau^{-1}(T,P)$ in Figure 8 is quite similar to that reported by Wu et al. in Rb$_2$GeF$_6$:Mn^{4+}.[53] That work explained the temperature dependence of the PL lifetime by considering independent contributions from $^4T_{2g}$ and ^2E_g states in Boltzmann equilibrium, and a nonradiative thermal

activation term, which is not explicitly included in the model but seems to be taken into account in the fitting of $\tau^{-1}(T,P)$ data (see eq 2 and Figure 3 of Wu et al.[53]). However, that work and in general most works related to the temperature dependence of Mn^{4+} PL lack comparison of both $\tau^{-1}(T,P)$ and $I_{PL}(T,P)$ data with the same equation to check model consistency.[29,40,46,53,54,61,62,64]

It is worth noting that the temperature dependence of the PL intensity in Mg$_2$TiO$_4$:0.1% Mn^{4+} does not match the quantum yield variations as deduced from $\tau(T)$ (eq 1), as it is shown in Figure 5b. The rapid decrease of $I_{PL}(T)$ with respect to what is expected on the basis of eq 1 unravels an additional nonradiative channel affecting the pumping efficiency of the $^4T_{2g}$ state but not the emitting ^2E_g state. This phenomenon occurs in Mg$_2$TiO$_4$:0.1% Mn^{4+} as the crossover point of the $^4T_{2g}$ and $^4A_{2g}$ states is close to the $^4T_{2g}$ minimum as it can be observed in the configurational coordinate model in Figure 9. The curvature of the parabola (d^2E/dQ^2) has been scaled to the force constant of the A$_{1g}(\nu_1)$ local mode of MnO$_6$ derived through its frequency in the $^4A_{2g}$ ground state (632 cm^{-1}— 78.4 meV—from emission) and $^4T_{2g}$ excited state (484 cm^{-1}—600 meV—in excitation).[19] The excited-state frequency for the spin-flip ^2E_g is taken as the ground-state frequency. Note that these local frequencies do not necessarily coincide with the corresponding Raman frequencies as Raman mainly probes the host TiO$_6$ rather than MnO$_6$ local modes (Table 1). Under such conditions, multiphonon relaxation processes from $^4T_{2g}$ to either ^2E_g or $^4A_{2g}$ directly compete with each other. If we describe this phenomenon in terms of the $^4T_{2g} \rightarrow {}^2E_g$ and $^4T_{2g} \rightarrow {}^4A_{2g}$ multiphonon transfer probabilities, then the total de-excitation probability is given by

$$\tau_{^4T_{2g}}^{-1} = \tau_{^2E_g}^{-1} e^{-E_1/k_B T} + \tau_{nr}^{-1} e^{-E_2/k_B T} \tag{10}$$

thus the pumping population efficiency of the ^2E_g state from $^4T_{2g}$ is

$$\phi_{\text{pumping}} = \frac{\tau_{^2E_g}^{-1}\, e^{-E_1/k_BT}}{\tau_{^2E_g}^{-1}\, e^{-E_1/k_BT} + \tau_{\text{nr}}^{-1}\, e^{-E_2/k_BT}} = \frac{1}{1 + p\, e^{-E_{^4T_{2g}}}}$$

(11)

where the effective activation energy is $E_{^4T_{2g}} = E_2 - E_1$. If we include this pumping efficiency mechanism, then the variation of $I_{\text{PL}}(T)$ becomes

$$I_{\text{PL}} = C \frac{\tau_0^{-1}\, \coth\left(\frac{\hbar\omega}{2k_BT}\right)^{3/2}}{\tau_0^{-1}\, \coth\left(\frac{\hbar\omega}{2k_BT}\right) + \tau_1^{-1}\, e^{-E_{\text{act}}/k_BT}} \frac{1}{1 + p \cdot e^{-E_{^4T_{2g}}/k_BT}}$$

(12)

The last fraction accounts for the multiphonon relaxation of the $^4T_{2g}$ state into ^2E_g besides direct relaxation into $^4A_{2g}$ ground state (ϕ_{pumping} in eq 4). Here, $E_{^4T_{2g}}$ is the activation energy associated with the pumping efficiency and the hyperbolic cotangent function involves the odd-parity activation term as in the lifetime, and also the effective excitation that is modulated by changes of the absorption cross section due to thermal band broadening. Both broadening and direct multiphonon relaxation into the $^4A_{2g}$ ground state determine the pumping efficiency η_{pumping} that is crucial to explain the uncorrelated behavior of $\tau(T)$ and $I_{\text{PL}}(T)$ in this Mn^{4+} phosphor. The fitted curve in Figure 5 corresponds to the pumping parameters of $E_{^4T_{2g}} = 0.15$ eV and $p = 493$. Nevertheless, this important result is behind some temperature-dependent studies of the PL intensity in other oxide phosphors, where intensity and lifetime data are barely compared. Different studies on Mn^{4+} PL[42,64–66] show examples where the pumping efficiency can depend on temperature through thermal activation processes yielding direct nonradiative de-excitation within $^4T_{2g}$ prior to relaxation into the emitting ^2E_g state. For this purpose, correlations between spectroscopic and excited-state dynamics data are worth investigating for phosphor modeling. In particular, the present result establishes guides to be followed to enhance pumping efficiency in Mn^{4+} systems on the basis of keeping the $^4T_{2g}$–$^4A_{2g}$ crossover point apart from the $^4T_{2g}$ energy minimum. According to pressure data, a reduction of the Mn–O bond length within the host crystal would definitely contribute to enhance both quantum and pumping efficiencies, and thus phosphor performance.

CONCLUSIONS

We have shown that singly Mn-doped $Mg_2Ti_{1-x}Mn_xO_4$ synthesized by solid-state reaction method yields formation of Mn^{3+} and Mn^{4+} ions. Although the presence of Mn^{3+} does not influence the PL dynamics of Mn^{4+}, it reduces the relative Mn^{4+} concentration for a given nominal concentration, x, and therefore on its PL intensity.

Codoping with Bi^{3+} and/or Li^+ enhances the photoluminescence efficiency of the Mn^{4+}-based phosphor due to oscillator-strength enhancement—pumping efficiency—of the $^4A_{2g} \rightarrow {}^4T_{2g}$ and $^4T_{1g}$ by the loss of center of inversion at Mn^{4+} due to the presence of neighboring Bi^{3+} and/or Li^+ and the stabilization of the Mn^{4+} following results obtained by Qiu et al.[28]

$Mg_2Ti_{1-x}Mn_xO_4$ spinel structure is stable up 14 GPa; above this pressure, this phase coexists with a new tetragonal phase.

The excitation and strong-field emission transition energies shift with pressure according to expectations on the basis of the Tanabe–Sugano diagram for a strong field d^3 ion with $\Delta/B = 25.6$ ($\Delta = 2.56$ eV; $B = 0.100$ eV), where pressure reduces the Mn–O length yielding the increase of Δ/B. We showed that the Mn–O bond is stiffer than the host-site Ti–O bond, giving rise to unusual dependences of $\Delta(R)$.

We have developed a dynamical model for explaining both the PL lifetime and PL intensity variations with pressure and temperature. The uncorrelated $\tau(T)$ and $I_{\text{PL}}(T)$ variations can now be explained by introducing a new nonradiative de-excitation channel directly from $^4T_{2g} \rightarrow {}^4A_{2g}$ by multiphonon relaxation in competition with the relaxation to the ^2E_g emitting state. The model is supported by the spectroscopic-obtained configurational coordinate model that foresees a $^4T_{2g}$–$^4A_{2g}$ crossover point near the $^4T_{2g}$ configurational energy minimum.

The model together with experimental data indicates that efficient Mn^{4+}-based phosphor can be obtained using host materials providing noncentrosymmetric sites for Mn^{4+} and shorter Mn–O bond lengths.
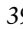
AUTHOR INFORMATION

Corresponding Authors

Enrique Jara − *MALTA TEAM, DCITIMAC, Facultad de Ciencias, Universidad de Cantabria, 39005 Santander, Spain*; Email: enrique.jara@unican.es

Fernando Rodríguez − *MALTA TEAM, DCITIMAC, Facultad de Ciencias, Universidad de Cantabria, 39005 Santander, Spain*; orcid.org/0000-0002-7237-7443; Email: rodriguf@unican.es

Authors

Rafael Valiente − *Dpto. Física Aplicada, Nanomedicine Group, Facultad de Ciencias, Universidad de Cantabria, 39005 Santander, Spain*; orcid.org/0000-0001-9855-8309

Marco Bettinelli − *Luminescent Materials Laboratory, Department of Biotechnology, University of Verona and INSTM, UdR Verona, 37134 Verona, Italy*; orcid.org/0000-0002-1271-4241

Complete contact information is available at:
https://pubs.acs.org/10.1021/acs.jpcc.1c08006

Notes

The authors declare no competing financial interest.

REFERENCES

(1) Schubert, E. F.; Kim, J. K. Solid-state light sources getting smart. *Science* **2005**, *308*, 1274–1278.

(2) Jüstel, T.; Nikol, H.; Ronda, C. New developments in the field of luminescent materials for lighting and displays. *Angew. Chem., Int. Ed.* **1998**, *37*, 3084–3103.

(3) Dai, Q.; Foley, M. E.; Breshike, C. J.; Lita, A.; Strouse, G. F. Ligand-passivated Eu:Y$_2$O$_3$ nanocrystals as a phosphor for white light emitting diodes. *J. Am. Chem. Soc.* **2011**, *133*, 15475–15486.

(4) Höppe, H. A. Recent developments in the field of inorganic phosphors. *Angew. Chem., Int. Ed.* **2009**, *48*, 3572−3582.

(5) Feldmann, C.; Jüstel, T.; Ronda, C. R.; Schmidt, P. J. Inorganic luminescent materials: 100 years of research and application. *Adv. Funct. Mater.* **2003**, *13*, 511−516.

(6) Kim, H.-s.; Brueckner, E.; Song, J.; Li, Y.; Kim, S.; Lu, C.; Sulkin, J.; Choquette, K.; Huang, Y.; Nuzzo, R. G.; et al. Unusual strategies for using indium gallium nitride grown on silicon (111) for solid-state lighting. *Proc. Natl. Acad. Sci. U.S.A.* **2011**, *108*, 10072−10077.

(7) Nakamura, S.; Senoh, M.; Mukai, T. High-power InGaN/GaN double-heterostructure violet light emitting diodes. *Appl. Phys. Lett.* **1993**, *62*, 2390−2392.

(8) Nakamura, S.; Mukai, T.; Senoh, M. Candela-class high-brightness InGaN/AlGaN double-heterostructure blue-light-emitting diodes. *Appl. Phys. Lett.* **1994**, *64*, 1687−1689.

(9) Chen, L.; Lin, C.-C.; Yeh, C.-W.; Liu, R.-S. Light converting inorganic phosphors for white light-emitting diodes. *Materials* **2010**, *3*, 2172−2195.

(10) Xie, R.-J.; Hirosaki, N.; Suehiro, T.; Xu, F.-F.; Mitomo, M. A simple, efficient synthetic route to $Sr_2Si_5N_8$:Eu^{2+}-based red phosphors for white light-emitting diodes. *Chem. Mater.* **2006**, *18*, 5578−5583.

(11) Xie, R.-J.; Hirosaki, N. Silicon-based oxynitride and nitride phosphors for white LEDs—A review. *Sci. Technol. Adv. Mater.* **2007**, *8*, 588.

(12) Lin, C. C.; Liu, R.-S. Advances in phosphors for light-emitting diodes. *J. Phys. Chem. Lett.* **2011**, *2*, 1268−1277.

(13) Setlur, A. A.; Heward, W. J.; Hannah, M. E.; Happek, U. Incorporation of Si^{4+}-$N^{3−}$ into Ce^{3+}-doped garnets for warm white LED phosphors. *Chem. Mater.* **2008**, *20*, 6277−6283.

(14) Wang, L.; Zhang, X.; Hao, Z.; Luo, Y.; Zhang, L.; Zhong, R.; Zhang, J. Interionic Energy Transfer in $Y_3Al_5O_{12}$:Ce^{3+}, Pr^{3+}, Cr^{3+} Phosphor. *J. Electrochem. Soc.* **2012**, *159*, F68.

(15) Zeuner, M.; Hintze, F.; Schnick, W. Low temperature precursor route for highly efficient spherically shaped LED-phosphors $M_2Si_5N_8$:Eu^{2+} (M= Eu, Sr, Ba). *Chem. Mater.* **2009**, *21*, 336−342.

(16) Piao, X.; Horikawa, T.; Hanzawa, H.; Machida, K.-i. Characterization and luminescence properties of $Sr_2Si_5N_8$:Eu^{2+} phosphor for white light-emitting-diode illumination. *Appl. Phys. Lett.* **2006**, *88*, No. 161908.

(17) Park, W. B.; Singh, S. P.; Yoon, C.; Sohn, K.-S. Combinatorial chemistry of oxynitride phosphors and discovery of a novel phosphor for use in light emitting diodes, $Ca_{1.5}Ba_{0.5}Si_5N_6O_3$:$Eu^{2+}$. *J. Mater. Chem. C* **2013**, *1*, 1832−1839.

(18) Ye, T.; Li, S.; Wu, X.; Xu, M.; Wei, X.; Wang, K.; Bao, H.; Wang, J.; Chen, J. Sol-gel preparation of efficient red phosphor Mg_2TiO_4:Mn^{4+} and EXAFS investigation on the substitution of Mn^{4+} for Ti^{4+}. *J. Mater. Chem. C* **2013**, *1*, 4327−4333.

(19) Adachi, S. Review—Mn^{4+}-Activated Red and Deep Red-Emitting Phosphors. *ECS J. Solid State Sci. Technol.* **2020**, *9*, No. 016001.

(20) Chen, D.; Zhou, Y.; Zhong, J. A review on Mn^{4+} activators in solids for warm white light-emitting diodes. *RSC Adv.* **2016**, *6*, 86285−86296.

(21) Lian, S.; Qi, Y.; Rong, C.; Yu, L.; Zhu, A.; Yin, D.; Liu, S. Effectively leveraging solar energy through persistent dual red phosphorescence: Preparation, characterization, and density functional theory study of $Ca_2Zn_4Ti_{16}O_{38}$:Pr^{3+}. *J. Phys. Chem. C* **2010**, *114*, 7196−7204.

(22) Zhongfei, M. U.; Yihua, H.; Guifang, J. Luminescence properties of Eu^{3+} and Ho^{3+} in Sr_2TiO_4. *J. Rare Earths* **2012**, *30*, 744−747.

(23) Zeng, P.-j.; Yu, L.-p.; Qiu, Z.-x.; Zhang, J.-l.; Rong, C.-y.; Li, C.-z.; Fu, Z.-h.; Lian, S.-x. Significant enhancement of luminescence intensity of $CaTiO_3$:Eu^{3+} red phosphor prepared by sol-gel method and co-doped with Bi^{3+} and Mg^{2+}. *J. Sol-Gel Sci. Technol.* **2012**, *64*, 315−323.

(24) Shannon, R. D. Revised effective ionic radii and systematic studies of interatomic distances in halides and chalcogenides. *Acta Crystallogr., Sect. A* **1976**, *32*, 751−767.

(25) Shim, J.-H.; Cho, N.-H.; Lee, S. Synthesis and characterization of Mg_2TiO_4-coated $LiCoO_2$ as a cathode material for lithium ion batteries. *Electrochim. Acta* **2017**, *243*, 162−169.

(26) Flot, D.; Irvine, J. Synthesis, electrical properties and thermal analysis of transition metal-doped Mg_2TiO_4 spinels. *Solid State Ionics* **2000**, *135*, 513−518.

(27) Hu, G.; Hu, X.; Chen, W.; Cheng, Y.; Liu, Z.; Zhang, Y.; Liang, X.; Xiang, W. Luminescence properties and thermal stability of red phosphor Mg_2TiO_4:Mn^{4+} additional Zn^{2+} sensitization for warm W-LEDs. *Mater. Res. Bull.* **2017**, *95*, 277−284.

(28) Qiu, Z.; Luo, T.; Zhang, J.; Zhou, W.; Yu, L.; Lian, S. Effectively enhancing blue excitation of red phosphor Mg_2TiO_4:Mn^{4+} by Bi^{3+} sensitization. *J. Lumin.* **2015**, *158*, 130−135.

(29) Long, J.; Ma, C.; Wang, Y.; Yuan, X.; Du, M.; Ma, R.; Wen, Z.; Zhang, J.; Cao, Y. Luminescent performances of Mn^{4+} ions during the phase evolution from $MgTiO_3$ to Mg_2TiO_4. *Mater. Res. Bull.* **2017**, *85*, 234−239.

(30) Lutterotti, L. Maud: a Rietveld analysis program designed for the internet and experiment integration. *Acta Crystallogr., Sect. A: Found. Crystallogr.* **2000**, *56*, s54.

(31) Shen, G.; Wang, Y.; Dewaele, A.; Wu, C.; Fratanduono, D. E.; Eggert, J.; Klotz, S.; Dziubek, K. F.; Loubeyre, P.; Fat'yanov, O. V.; et al. Toward an international practical pressure scale: A proposal for an IPPS ruby gauge (IPPS-Ruby2020). *High Pressure Res.* **2020**, *40*, 299−314.

(32) Klotz, S.; Chervin, J.; Munsch, P.; Le Marchand, G. Hydrostatic limits of 11 pressure transmitting media. *J. Phys. D: Appl. Phys.* **2009**, *42*, No. 075413.

(33) Brunold, T.; Güdel, H.; Kück, S.; Huber, G. Excited-state absorption and laser potential of Mn^{6+}-doped $BaSO_4$ crystals. *J. Opt. Soc. Am. B* **1997**, *14*, 2373−2377.

(34) Romanyuk, Y.; Ehrentraut, D.; Pollnau, M.; García-Revilla, S.; Valiente, R. Low-temperature flux growth of sulfates, molybdates, and tungstates of Ca, Sr, and Ba and investigation of doping with Mn^{6+}. *Appl. Phys. A* **2004**, *79*, 613−618.

(35) Schuyt, J.; Williams, G. Optical properties of Mn^{2+} doped $CsCdF_3$: A potential real-time and retrospective UV and X-ray dosimeter material. *J. Appl. Phys.* **2019**, *125*, No. 233102.

(36) Burns, R. G. *Mineralogical Applications of Crystal Field Theory*, 2nd ed.; Cambridge Topics in Mineral Physics and Chemistry; Cambridge University Press, 1993.

(37) Wang, Y.; Lei, H.; Jiang, P.; Liu, L.; Cui, K.; Cao, W. Synthesis and optical properties of intense blue colors oxides based on Mn^{5+} in tetrahedral sites in $Ba_7Al_{2−x}Mn_xO_{10+y}$. *Ceram. Int.* **2021**, *47*, 686−691.

(38) Gómez-Salces, S.; Barreda-Argüeso, J. A.; Valiente, R.; Rodríguez, F. A study of Ce^{3+} to Mn^{2+} energy transfer in high transmission glasses using time-resolved spectroscopy. *J. Mater. Chem. C* **2016**, *4*, 9021−9026.

(39) Kück, S.; Hartung, S.; Hurling, S.; Petermann, K.; Huber, G. Optical transitions in Mn^{3+}-doped garnets. *Phys. Rev. B* **1998**, *57*, 2203.

(40) Adachi, S. Mn^{4+} vs Cr^{3+}: A comparative study as activator ions in red and deep red-emitting phosphors. *ECS J. Solid State Sci. Technol.* **2020**, *9*, No. 026003.

(41) Zhang, S.; Hu, Y. Photoluminescence spectroscopies and temperature-dependent luminescence of Mn^{4+} in $BaGe_4O_9$ phosphor. *J. Lumin.* **2016**, *177*, 394−401.

(42) Zhou, Q.; Dolgov, L.; Srivastava, A. M.; Zhou, L.; Wang, Z.; Shi, J.; Dramićanin, M. D.; Brik, M. G.; Wu, M. Mn^{2+} and Mn^{4+} red phosphors: synthesis, luminescence and applications in WLEDs. A review. *J. Mater. Chem. C* **2018**, *6*, 2652−2671.

(43) Henderson, B.; Imbush, G. *Optical Spectroscopy of Inorganic Solids*; Clarendon Press: Oxford, 1989.

(44) Sánchez-Alejo, M. A.; Rodríguez, F.; Barreda-Argüeso, J.; Camarillo, I.; Jaque, F.; Flores, C.; Murrieta, H.; Hernández, J.; Camarillo, E. Photoluminescence study of $LiNbO_3$:Cr^{3+}; W^{4+} at high pressure. Pressure dependence of spectroscopic parameters and local structure of Cr^{3+}. *Opt. Mater.* **2016**, *60*, 94−100.

(45) Li, X.; Jiang, G.; Zhou, S.; Wei, X.; Chen, Y.; Duan, C. K.; Yin, M. Luminescent properties of chromium (III)-doped lithium aluminate for temperature sensing. *Sens. Actuators, B* **2014**, *202*, 1065−1069.

(46) Srivastava, A. M.; Brik, M. G.; Camardello, S. J.; Comanzo, H. A.; Garcia-Santamaria, F. Optical spectroscopy and crystal field studies of the Mn^{4+} ion ($3d^3$) in the double perovskite $NaLaMgTeO_6$. *Z. Naturforsch. B* **2014**, *69*, 141−149.

(47) Brik, M. G.; Srivastava, A. M. Electronic energy levels of the Mn^{4+} ion in the perovskite, $CaZrO_3$. *ECS J. Solid State Sci. Technol.* **2013**, *2*, R148.

(48) Griffith, J. S. *The Theory of Transition-Metal Ions*; Cambridge University Press, 1964.

(49) Hernández, I.; Rodríguez, F.; Hochheimer, H. Pressure-induced two-color photoluminescence in MnF_2 at room temperature. *Phys. Rev. Lett.* **2007**, *99*, No. 027403.

(50) Quintanilla, M.; Cantelar, E.; Cussó, F.; Barreda-Argüeso, J.; González, J.; Valiente, R.; Rodríguez, F. Control of infrared cross-relaxation in $LiNbO_3:Tm^{3+}$ through high-pressure. *Opt. Mater. Express* **2015**, *5*, 1168−1182.

(51) Han, M.; Tang, H.; Liu, L.; Wang, Y.; Zhang, X.; Lv, L. Tuning the Mn^{4+} Coordination Environment in Mg_2TiO_4 through a Codoping Strategy for Enhancing Luminescence Performance. *J. Phys. Chem. C* **2021**, 15687−15695.

(52) Rodríguez, F.; Hernandez, I.; Moreno, M.; Alcala, R. Photoluminescence and radiationless processes in Mn^{2+}-doped $Ca_{1−x}Sr_xF_2$ fluorites as a function of pressure and temperature. A structural correlation study. *J. Chem. Phys.* **2003**, *119*, 8686−8694.

(53) Wu, W.-L.; Fang, M.-H.; Zhou, W.; Lesniewski, T.; Mahlik, S.; Grinberg, M.; Brik, M. G.; Sheu, H.-S.; Cheng, B.-M.; Wang, J.; et al. High color rendering index of $Rb_2GeF_6:Mn^{4+}$ for light-emitting diodes. *Chem. Mater.* **2017**, *29*, 935−939.

(54) Wang, C.-P.; Shieh, S. R.; Withers, A. C.; Liu, X.; Zhang, D.; Tkachev, S. N.; Djirar, A.-E.; Xie, T.; Rumney, J. D. Raman and X-ray diffraction study of pressure-induced phase transition in synthetic Mg_2TiO_4. *Sci. Rep.* **2020**, *10*, No. 6278.

(55) Hazen, R. M.; Yang, H. Effects of cation substitution and order-disorder on PVT equations of state of cubic spinels. *Am. Mineral.* **1999**, *84*, 1956−1960.

(56) Sugano, S.; Tanabe, Y.; Kamimura, H. *Multiplets of Transition-Metal Ions in Crystals*; Academic Press: New York, 1970.

(57) Rodríguez, F.; Moreno, M. Dependence of the optical spectrum of $MnF_6^{4−}$ on the Mn^{2+}-$F^−$ distance. *J. Chem. Phys.* **1986**, *84*, 692−697.

(58) Barreda-Argüeso, J. A.; Aguado, F.; González, J.; Valiente, R.; Nataf, L.; Sanz-Ortiz, M. N.; Rodríguez, F. Crystal-Field Theory Validity Through Local (and Bulk) Compressibilities in CoF_2 and $KCoF_3$. *J. Phys. Chem. C* **2016**, *120*, 18788−18793.

(59) Barreda-Argüeso, J. A.; Rodríguez, F. Pressure dependence of the crystal-field spectrum of $KNiF_3$: Single and double excitations. *Phys. Rev. B* **2021**, *103*, No. 085115.

(60) Martín-Rodríguez, R.; Valiente, R.; Rodríguez, F.; Bettinelli, M. Temperature and pressure dependence of the optical properties of Cr^{3+}-doped $Gd_3Ga_5O_{12}$ nanoparticles. *Nanotechnology* **2011**, *22*, No. 265707.

(61) Zhang, J.; Zhai, J.; Chou, X.; Shao, J.; Lu, X.; Yao, X. Microwave and infrared dielectric response of tunable $Ba_{1−x}Sr_xTiO_3$ ceramics. *Acta Mater.* **2009**, *57*, 4491−4499.

(62) Zhang, J.; Zhai, J.; Wang, J.; Shao, J.; Lu, X.; Yao, X. Infrared dielectric response and Raman spectra of tunable $Ba_{0.5}Sr_{0.5}TiO_3$−Mg_2TiO_4 composite ceramics. *J. Appl. Phys.* **2010**, *107*, No. 014106.

(63) Sanz-Ortiz, M. N.; Rodriguez, F.; Hernández, I.; Valiente, R.; Kück, S. Origin of the $^2E \leftrightarrow \, ^4T_2$ Fano resonance in Cr^{3+}-doped $LiCaAlF_6$: Pressure-induced excited-state crossover. *Phys. Rev. B* **2010**, *81*, No. 045114.

(64) Beers, W.; Smith, D.; Cohen, W.; Srivastava, A. Temperature dependence (13-600 K) of Mn^{4+} lifetime in commercial $Mg_{28}Ge_{7.55}O_{32}F_{15.04}$ and K_2SiF_6 phosphors. *Opt. Mater.* **2018**, *84*, 614−617.

(65) Dramićanin, M. D.; Milićević, B.; Dordević, V.; Ristić, Z.; Zhou, J.; Milivojević, D.; Papan, J.; Brik, M. G.; Ma, C.-G.; Srivastava, A. M.; et al. $Li_2TiO_3:Mn^{4+}$ Deep-Red Phosphor for the Lifetime-Based Luminescence Thermometry. *ChemistrySelect* **2019**, *4*, 7067−7075.

(66) Senden, T.; van Dijk-Moes, R. J.; Meijerink, A. Quenching of the red Mn^{4+} luminescence in Mn^{4+}-doped fluoride LED phosphors. *Light: Sci. Appl.* **2018**, *7*, No. 8.